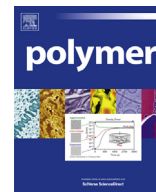




Contents lists available at ScienceDirect

Polymer

journal homepage: www.elsevier.com/locate/polymer

Observation of constraint surface dynamics of polystyrene thin films by functionalization of a silsesquioxane cage

Taiki Hoshino ^{a, b, *}, Shiki Nojima ^{a, c}, Masanao Sato ^c, Tomoyasu Hirai ^{a, c, d, e},
Yuji Higaki ^{a, c, d, e, f}, So Fujinami ^a, Daiki Murakami ^{d, f}, Shigesaburo Ogawa ^f,
Hiroshi Jinnai ^{f, g}, Atsushi Takahara ^{a, c, d, e, f}, Masaki Takata ^{a, g}

^a RIKEN SPring-8 Center, 1-1-1 Kouto, Sayo-cho, Sayo-gun, Hyogo 679-5148, Japan

^b JST-PRESTO, Tokyo Institute of Technology, 4259 Nagatsuta, Midori-ku, Yokohama, Kanagawa 226-8502, Japan

^c Graduate School of Engineering, Kyushu University, Japan

^d Institute for Materials Chemistry and Engineering, Kyushu University, 744 Motoooka, Nishi-ku, Fukuoka 819-0395, Japan

^e International Institute for Carbon-Neutral Energy Research (WPI-I2CNER), Kyushu University, 744 Motoooka, Nishi-ku, Fukuoka 819-0395, Japan

^f JST, ERATO Takahara Soft Interfaces Project, Kyushu University, 744 Motoooka, Nishi-ku, Fukuoka 819-0395, Japan

^g Institute of Multidisciplinary Research for Advanced Materials (IMRAM), Tohoku University, 2-1-1 Katahira, Aoba-ku, Sendai 980-8577, Japan

ARTICLE INFO

Article history:

Received 18 May 2016

Received in revised form

9 August 2016

Accepted 11 August 2016

Available online xxx

Keywords:

Capillary wave

Polymer thin film

X-ray photon correlation spectroscopy

ABSTRACT

The surface dynamics of polyhedral oligomeric silsesquioxane (POSS)-functionalized polystyrene (PS-POSS) thin films above the glass transition temperature were studied by grazing-incidence X-ray photon correlation spectroscopy in order to elucidate the effects of POSS at the end of the polystyrene chains. Much slower fluctuations were observed in the surface of PS-POSS thin films than in the polystyrene thin films, despite the negligible difference in their bulk viscosity. Quantitative analysis based on fluctuation-dissipation theorem indicated that there is a high-viscosity layer at the surface of the PS-POSS films, and that the substrate interface originated from POSS segregation.

© 2016 Elsevier Ltd. All rights reserved.

1. Introduction

The stability of polymer thin films is important in applications such as coatings and dielectric layers. Various methods of inhibiting dewetting of the layers have been developed, such as modifying the substrate, adding a nanofiller, and cross-linking the polymer [1–4]. Adding polyhedral oligomeric silsesquioxanes (POSS) to thin films is an efficient way to prevent them from dewetting. For example, Hosaka et al. stabilized polystyrene (PS) thin films by inhibiting dewetting with dispersed phenethyl-POSS and octacyclopentyl-POSS [5,6]. Miyamoto et al. also observed the inhibition of dewetting using octacyclopentyl-POSS-terminated PS thin films (PS-POSS) [7]. Miyamoto et al. found that the low molecular weight PS-POSS ($M_n \approx 2000$) produced a large difference in the dewetting behavior, whereas the high molecular weight analog ($M_n \approx 40,000$) produced a small difference [7]. They investigated the structures of

thin films by neutron reflectivity measurements, and discussed the suppression of dewetting in terms of the segregation of POSS at the surface and at the substrate interface. However, the question of how the segregation of POSS affects the inhibition of dewetting remains unsettled. To answer this fundamental question, the physical properties, such as viscosity and surface tension, of PS-POSS thin films rather than bulk PS-POSS should be examined.

Above the glass transition temperature, thermally agitated capillary waves are generated and damped continually at the surface of polymer thin films. The capillary wave spectra for homogeneous liquids have been studied by fluctuation-dissipation theorem, and they were described by using the viscosity, surface tension, and density in the thin films [8,9]. The dynamics of capillary waves have been experimentally studied by coherent scattering techniques, such as surface dynamic light scattering [10,11] and grazing-incidence X-ray photon correlation spectroscopy (GI-XPCS) [12–17]. Kim et al. performed GI-XPCS for linear PS thin films, and observed the capillary waves as predicted by the hydrodynamic theory for homogeneous thin films with bulk viscosity [18]. The unique properties of the thin films can be determined by

* Corresponding author. RIKEN SPring-8 Center, 1-1-1 Kouto, Sayo-cho, Sayo-gun, Hyogo 679-5148, Japan.

E-mail address: t-hoshino@spring8.or.jp (T. Hoshino).

the dynamical behavior of capillary waves on the films. Wang et al. measured the surface fluctuations of branched-polymer thin films and found that the viscosities calculated from the capillary wave spectra of thin films were 100 times higher than in the bulk [16]. Jiang et al. considered the dynamics of bilayer as a representative example of inhomogeneous thin films, and calculated the surface and interfacial dynamics of polymeric liquid bilayer films based on fluctuation-dissipation theorem [19].

The dynamics of the capillary waves reflects the physical properties of thin films in thin film conditions, and thus the inhomogeneity of thin films can be discussed by investigating the dynamics of capillary waves. In this study, we investigated the capillary waves on PS and PS-POSS thin films with different molecular weights ($M_n = 40k$, $25k$, and $2.3k$) by using GI-XPCS. For high molecular weight polymers ($M_n = 40k$ and $25k$), no major difference was observed between the PS and PS-POSS thin films, and the dynamics of the capillary waves were described by uniform viscosity and their viscosities were same as the bulk viscosity throughout the films. However, for low molecular weight polymers ($M_n = 2.3k$), unique behavior was observed for the PS-POSS thin films. The difference between the PS and PS-POSS films may originate from the non-uniform structure of the PS-POSS thin films. We quantitatively discuss the capillary wave dynamics of PS-POSS thin films based on the fluctuation-dissipation theorem and discuss the physical properties of the films.

2. Experimental

PS and PS-POSS were prepared via living anionic polymerization. Tetrahydrofuran was transferred to a flask and cooled to -78°C . After 5 min, *sec*-BuLi was added until the solution turned yellow. The flask was removed from the cooling bath and allowed to reach room temperature, upon which the solution became colorless. The solution was cooled to -78°C again, and 1.07 M *sec*-BuLi solution in hexane/cyclohexane was added. Styrene was added, turning the mixture orange. After polymerization, half of the reaction mixture was poured into a large amount of methanol to prepare proton-terminated PS (Fig. 1(a)). The other half was quenched with CO_2 to obtain carbonyl-terminated PS (PS-COOH), and precipitated in a large amount of methanol/HCl. The polymers were filtered and dried under vacuum at 100°C for 24 h. PS-POSS (Fig. 1(b)) was obtained by adding 1-(3-amino)propyl-3,5,7,9,11,13,15-isooctylpentacyclo[9.5.1.1^{3,9}.1^{5,15}.1^{7,13}]octasiloxane (POSS(isooctyl)) (Hybrid Plastics) and 1,4-dioxane, *N,N'*-dicyclohexylcarbodiimide to a 20 wt % solution of PS-COOH in 1,4-dioxane. The mixture was stirred at 50°C for 12 h, filtered, and then poured into a large amount of hexane. The residue was filtered and dried under vacuum at 100°C for 24 h. The molecular weight and POSS content of the PS and PS-POSS are summarized in Table 1. The molecular weight of the PS moieties of PS-POSS40k, PS-POSS25k, and PS-POSS2.3k were the same as for PS40k, PS25k, and PS2.3k, respectively, because they were obtained from the same mixture.

We investigated the dynamics of the surface fluctuation of PS and PS-POSS thin films with $M_n = 40k$, $25k$, and $2.3k$ spin-coated on silicon wafer substrates using cyclopentanone as a solvent. Prior to the film coating, the silicon wafer substrates were cleaned by piranha solution (H_2O_2 (30%)/ H_2SO_4 (70%) (v/v)) for 2 h, and rinsed with deionized water. Before the GI-XPCS measurements the thin films were annealed above the glass transition temperature for 24 h at 423 K for molecular weights of $25k$ and $40k$, and for 12 h at 383 K for the molecular weight of $2.3k$. No dewetting of thin films was observed after annealing and the GI-XPCS measurements.

The GI-XPCS measurements were performed on the BL19LXU beamline of SPring-8 with a 27-m-long undulator [20]. The

undulator source and Si(111) monochromator were tuned to an energy of 7.30 keV . The incident X-rays with transverse coherence of $16 \times 125\text{ }\mu\text{m}$ ($H \times V$) at the sample position were cut by slits with dimensions of $20 \times 20\text{ }\mu\text{m}$. The parasitic scattering was shielded by the other slits. The experimental geometry is illustrated schematically in Fig. 2. The sample was irradiated with partially coherent X-rays in a vacuum with an incident angle of 0.14° , which was below the critical angle for total external reflection. Direct and specular beam were hidden by beam-stop, and the off-specular diffuse scattering, in which exit angles $\sim 0.25\text{--}0.6^\circ$, from the polymer surface was recorded. The surface fluctuations in the irradiated area of polymer thin films were measured through the scattered X-rays. The scattered X-rays were detected by a two-dimensional hybrid pixel array detector (PILATUS 100K, DECTRIS) with a grid mask resolution enhancer (the effective detected area of each pixel is $\sim 45\text{ }\mu\text{m}$ in diameter) mounted $\sim 3.5\text{ m}$ downstream of the sample [21–23]. For the measurements, 5000–20,000 images were taken with an exposure time of 10–300 ms and a readout time of 3 ms. During the GI-XPCS measurements, the thin films with $M_n = 25k$ and $40k$ were kept at 413 K , and the thin films with $M_n = 2.3k$ were kept at 393 K . For investigating the thickness dependence, three different thickness of each polymer were measured: 50, 81, and 146 nm for PS40k; 50, 84, and 142 nm for PS-POSS40k; 44, 89, and 155 nm for PS25k; 44, 79, and 144 nm for PS-POSS25k; 47, 58, and 76 nm for PS2.3k; and 35, 52, and 61 nm for PS-POSS2.3k. The thicknesses were measured by an ellipsometer (MASS-103FH, Five lab.) or interferometer (Optical NanoGauge C11627, Hamamatsu Photonics).

During GI-XPCS measurements, the fluctuation of the scattering intensity, $I(\mathbf{q}, t)$, at a scattering vector \mathbf{q} , is obtained in a time series, t , and the intensity time-autocorrelation function $g_2(\mathbf{q}, t)$ is evaluated as

$$g_2(\mathbf{q}, t) = \langle I(\mathbf{q}, t')I(\mathbf{q}, t' + t) \rangle / \langle I(\mathbf{q}, t') \rangle^2, \quad (1)$$

where the angle brackets indicate time-averaging. In the evaluation, $g_2(\mathbf{q}, t)$ is averaged over all pixels within area belonging to $|\delta\mathbf{q}_\parallel| = 0.5 \times 10^{-3}\text{ nm}^{-1}$ where the vector \mathbf{q}_\parallel indicates the in-plane component of \mathbf{q} , $q_\parallel = |\mathbf{q}_\parallel| = \sqrt{q_x^2 + q_y^2}$. To check the radiation damage, all the $g_2(q_\parallel, t)$ for last 1000 frames were compared to that for first 1000 frames. In the present study, the deviations were small enough compared to error bars shown in figures later.

The glass transition temperature, T_g , was measured by differential scanning calorimetry with a calorimeter (EXSTRA DSC-6000, Seiko Instruments Inc.). The viscosities, η , of bulk polymers were measured by using a rotational rheometer (Physica MCR101, Anton Paar). To determine the surface tension, γ , the contact angles, θ , of four from the 1-alkyl-3-methylimidazolium bis(trifluoromethylsulfonyl)amide $[\text{C}_n\text{mim}][\text{Ntf}_2]$ ($n = 2, 4, 6, 10$) ionic liquids were measured on thin films of PS25k, PS40k, PS-POSS25k, and PS-POSS40k at 413 K and PS2.3k and PS-POSS2.3k at 393 K . γ was determined by linear extrapolation of the surface tension data of the ionic liquids [24] to $\cos\theta = 1$. The measured values of T_g , η , and γ are summarized in Tables 2 and 3.

X-ray photoelectron spectroscopy (XPS) depth profiles (PHI 5000 VersaProbe, ULVAC-PHI) were obtained with an Ar gas cluster ion beam gun (GCIB) with a monochromatic Al-K α X-ray source (1486.6 eV) [25,26]. The Ar GCIB gun was operated at a 2.5 kV accelerating voltage and a 5 nA beam current. The photoelectron take-off angle was maintained at 45° . High-resolution C 1s, Si 2p and O 1s spectra were acquired at 0.1 eV steps for PS-POSS2.3k (44-nm-thick), PS-POSS25k (105-nm-thick) and PS-POSS40k (120-nm-thick) thin films.

Grazing incidence small angle scattering (GI-SAXS) measurements were performed at BL45XU beamline in SPring-8 [27]. The

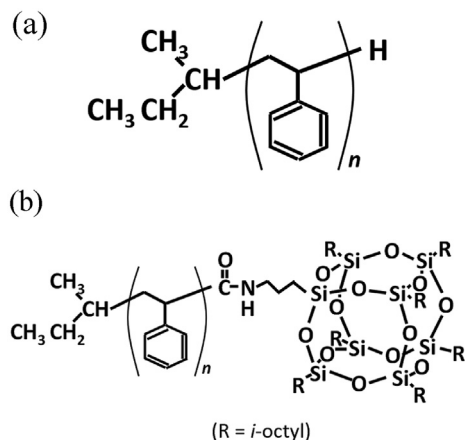


Fig. 1. Chemical structures of (a) PS and (b) PS-POSS.

energy of the X-ray beam was 12.40 keV, and the scattering profiles were obtained by two dimensional detector PILATUS 3×2 M (DECTRIS) mounted at 2567 mm downstream of the sample. The thin film samples were irradiated with an incident angle of 0.08° , which was below the critical angle for total external reflection. The geometry was almost same as Fig. 2 and the off-specular diffuse scattering was measured for PS-POSS2.3k (47-nm-thick), PS-POSS25k (78-nm-thick) and PS-POSS40k (47-nm-thick).

3. Results and discussion

A Static structure of PS-POSS thin films

To investigate the structure of our PS-POSS thin films, we performed Ar gas cluster sputtering XPS measurements. Fig. 3(a)–(c) show the XPS spectra for Si 2p from the thin films of PS-POSS2.3k, PS-POSS25k and PS-POSS40k sputtered by Ar gas cluster ion beam at sputter time of 0, 0.4, 0.8, 1.2 and 1.6 min, which corresponds to the depth from the surface of 0, 1.20, 2.39, 3.59 and 4.79 nm. At the surface (sputter time of 0 min) the peaks at ~ 101 eV were observed for all the PS-POSS thin films, and the intensity of the peaks became lower with increasing the sputter time. Fig. 3(d) shows the depth profile of the signal ratio of the XPS spectrum, $I_{\text{Si}2p}/I_{\text{C}1s}$, for PS-POSS2.3k, PS-POSS25k, and PS-POSS40k, where $I_{\text{Si}2p}$ and $I_{\text{C}1s}$ are the integrated area of the Si 2p peak and C 1s peak, respectively. $I_{\text{Si}2p}/I_{\text{C}1s}$ for all the films at the surfaces are higher than that of inside of the films. Furthermore $I_{\text{Si}2p}/I_{\text{C}1s}$ for PS-POSS2.3k near the surface is much higher than that for the other films. These results represent the enrichment of Si on the surfaces of all films, indicating the segregation of POSS at the surface. Moreover the POSS at the surface of PS-POSS2.3k thin film is more segregated than that of PS-POSS25k and PS-POSS40k thin films.

Regarding the structure of near substrate, the clear evidence of POSS segregation at the substrate was not obtained from the Si 2p

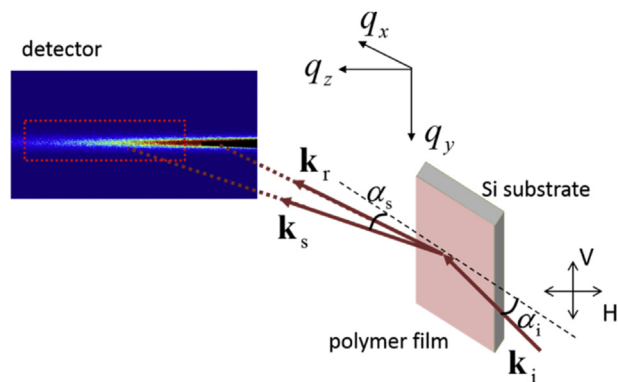


Fig. 2. Schematic experimental setup for GI-XPCS. (α_i and α_s are the incident and the scattered angles, respectively.) The red box in the detector shows the ranges of the wave vectors analyzed for dynamics of surface fluctuations. (For interpretation of the references to colour in this figure legend, the reader is referred to the web version of this article.)

spectra since the peaks for POSS could not be distinguished from the peaks for the substrate. Then we checked the spectra for O 1s. Fig. 4(a)–(c) show the XPS spectra for O 1s from the thin films of PS-POSS2.3k, PS-POSS25k and PS-POSS40k at various sputter time.

At the surface, sputter time of 0 min (depth = 0 nm), the peak at ~ 531 eV were observed for all the PS-POSS thin films while the apparent peak was not observed inside the films obtained at sputter time of 4.8 min. These peaks at ~ 531 eV can be assigned as POSS originating peak because they were not observed from a homo-PS thin film (data are not shown) at any sputter time but observed from only PS-POSS thin films. From the substrates, the peaks at ~ 532.5 eV, which originating from SiO_2 layer on the silicon substrate, were observed for all the thin films at enough large sputter time. The spectrum for the PS-POSS2.3k thin film at sputter time of 10.6 min, which corresponds to near the substrate, contains two peaks, originating from POSS and originating from the substrate. This result indicates POSS segregation in the thin films near the substrate. On the other hand, for PS-POSS25k and PS-POSS40k thin films, no apparent peak originating from POSS were observed near the substrate. Due to the low contents of POSS in PS-POSS25k and PS-POSS40k, the peak from POSS might be very small and negligible. Fig. 4(d) shows the depth profile of the signal ratio of the XPS spectrum, $I_{\text{O}1s}^{\text{POSS}}/I_{\text{C}1s}$, for PS-POSS2.3k, where $I_{\text{O}1s}^{\text{POSS}}$ is the integrated area of the O 1s peak originating from POSS at ~ 531 eV. This profile clearly shows POSS segregation at the surface and the near substrate.

The inplane structure of the surface of PS-POSS thin films were studied by GI-SAXS measurements. Fig. 5 shows the intensity profile against q_{\parallel} for PS-POSS2.3k, PS-POSS25k and PS-POSS40k thin films. The profile for PS-POSS2.3k multiplied by 0.5 was also plotted for comparison with the other profiles. These profiles showed similar curves, and no apparent features were observed indicating the inplane structure.

These results agree with the reported results from the neutron reflectivity measurements by Miyamoto et al. [7]. They studied the structure of PS-POSS thin films by the neutron reflectivity measurements of deuterated PS-POSS thin films, and they found that the POSS moieties of dPS-POSS formed an enrichment layer at the surface and the substrate interface. Furthermore, there was a dPS-rich layer between the POSS-rich layer and the center bulk layer.

Based on these results for PS-POSS thin films, schematic drawing of the structure of PS-POSS thin films could be depicted. Fig. 6(a) shows a schematic drawing of the low molecular weight PS-POSS ($M_n = 2.3k$) thin film. In this case PS-POSS thin films were

Table 1
Summary of molecular weights of PS and PS-POSS.

Sample	M_n	M_w/M_n	POSS content (wt%)
PS40k	39500	1.04	0
PS-POSS40k	39500	1.04	3.0
PS25k	2500	1.06	0
PS-POSS25k	25000	1.06	4.6
PS2.3k	2300	1.21	0
PS-POSS2.3k	2300	1.21	33.6

Table 2
 η , γ , and T_g of PS40k, PS-POSS40k, PS25k, and PS-POSS25k.

Sample	η (Pa s) (at 413 K)	γ (mN m ⁻¹) (at 413 K)	T_g (K)
PS40k	2.25×10^5	18.7	375
PS-POSS40k	2.21×10^5	17.7	375
PS25k	5.86×10^4	19.6	374
PS-POSS25k	5.75×10^4	1.4	374

Table 3
 η , γ , and T_g of PS2.3k and PS-POSS2.3k

Sample	η (Pa s) (at 393 K)	γ (mN m ⁻¹) (at 393 K)	T_g (K)
PS2.3k	1.09×10^3	21.2	348
PS-POSS2.3k	1.10×10^3	12.8	348

composed of a surface layer, bulk layer, and substrate interface layer. In the bulk layer, the PS-POSS chains were oriented randomly. In contrast, in the surface layer and the substrate interface layer, the PS-POSS chains were oriented perpendicularly, with the POSS part facing the air and the substrate. Fig. 6(b) shows a schematic drawing of the high molecular weight PS-POSS ($M_n = 25k$ and $40k$) thin films. The segregation of POSS could be much weaker than that

of PS-POSS2.3k thin films and the layer structure could be unclear.

B GI-XPCS for high molecular weight PS and PS-POSS thin films ($M_n = 25k$ and $40k$)

Fig. 7(a) shows representative data for the measured $g_2(q_{//}, t)$ of the high molecular weight PS and PS-POSS thin films. They were taken at $q_{//} = 7.74 \times 10^{-3} \text{ nm}^{-1}$ for PS25k and PS-POSS25k with thicknesses of 44 nm at 413 K. There were no clear differences between PS25k and PS-POSS25k.

The relaxation rates of $g_2(q_{//}, t)$ are evaluated by fitting to an exponential function,

$$g_2(q_{//}, t) = \beta \exp[-2\Gamma t] + 1, \quad (2)$$

where β is the speckle contrast and Γ is the relaxation rate. Typical values of β were 0.01–0.03 with a slight $q_{//}$ dependence, which was consistent with the estimated value from the speckle size and the hole size of the grid mask on the detector. Eq. (2) fits the experimental $g_2(q_{//}, t)$ data (solid lines, Fig. 7(a)) with $\Gamma = 3.73 \times 10^{-2}$ and $3.63 \times 10^{-2} \text{ s}^{-1}$ for PS25k and PS-POSS25k, respectively. The values of Γ for PS25k and PS-POSS25k obtained from the fitting analysis with Eq. (2) are plotted against $q_{//}$ in Fig. 7(b) and are similar over

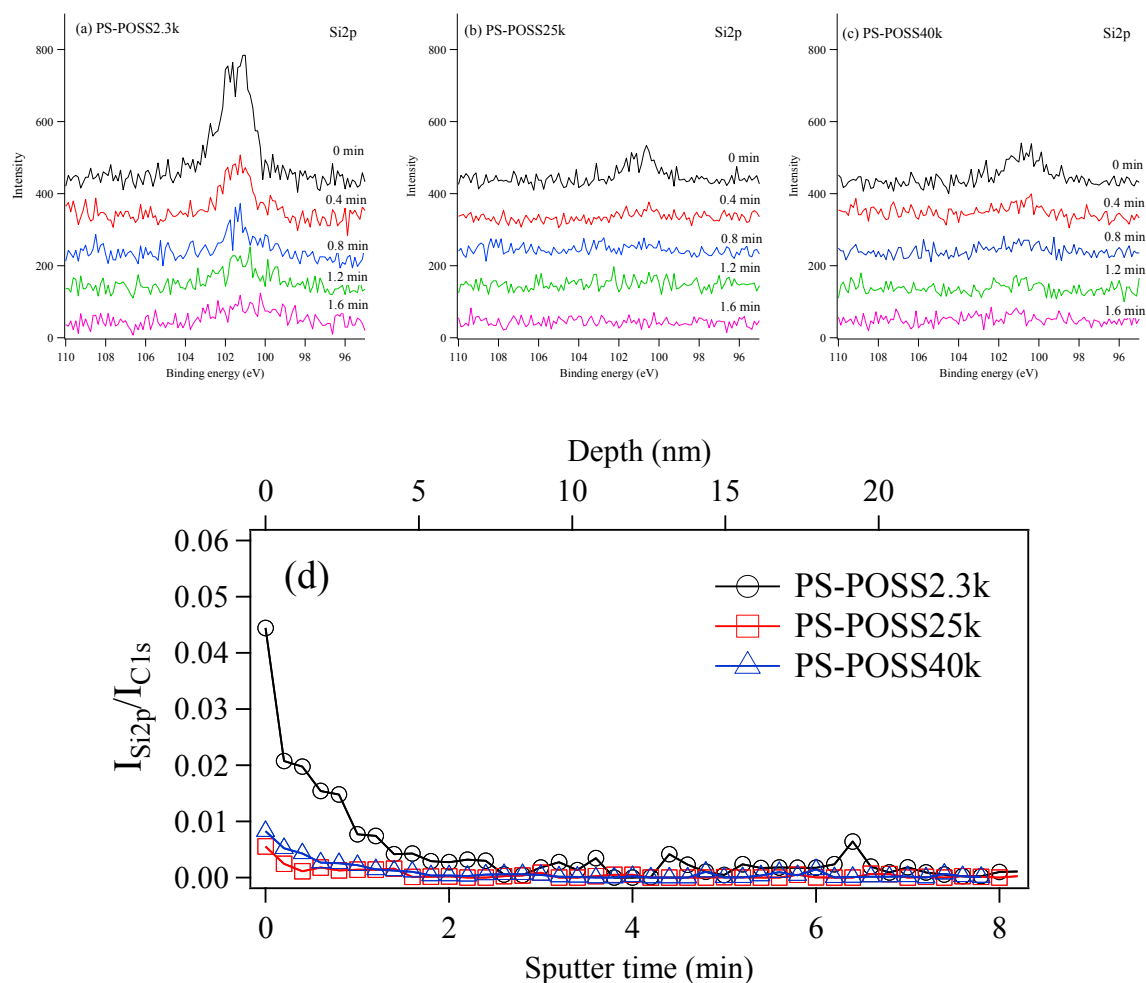


Fig. 3. XPS spectra of Si2p near surface of thin films of (a) PS-POSS2.3k, (b) PS-POSS25k and (c) PS-POSS40k sputtered by Ar gas cluster ion beam at various sputter time. (d) Depth profile of the signal ratio of Si2p to C1s for PS-POSS thin films.

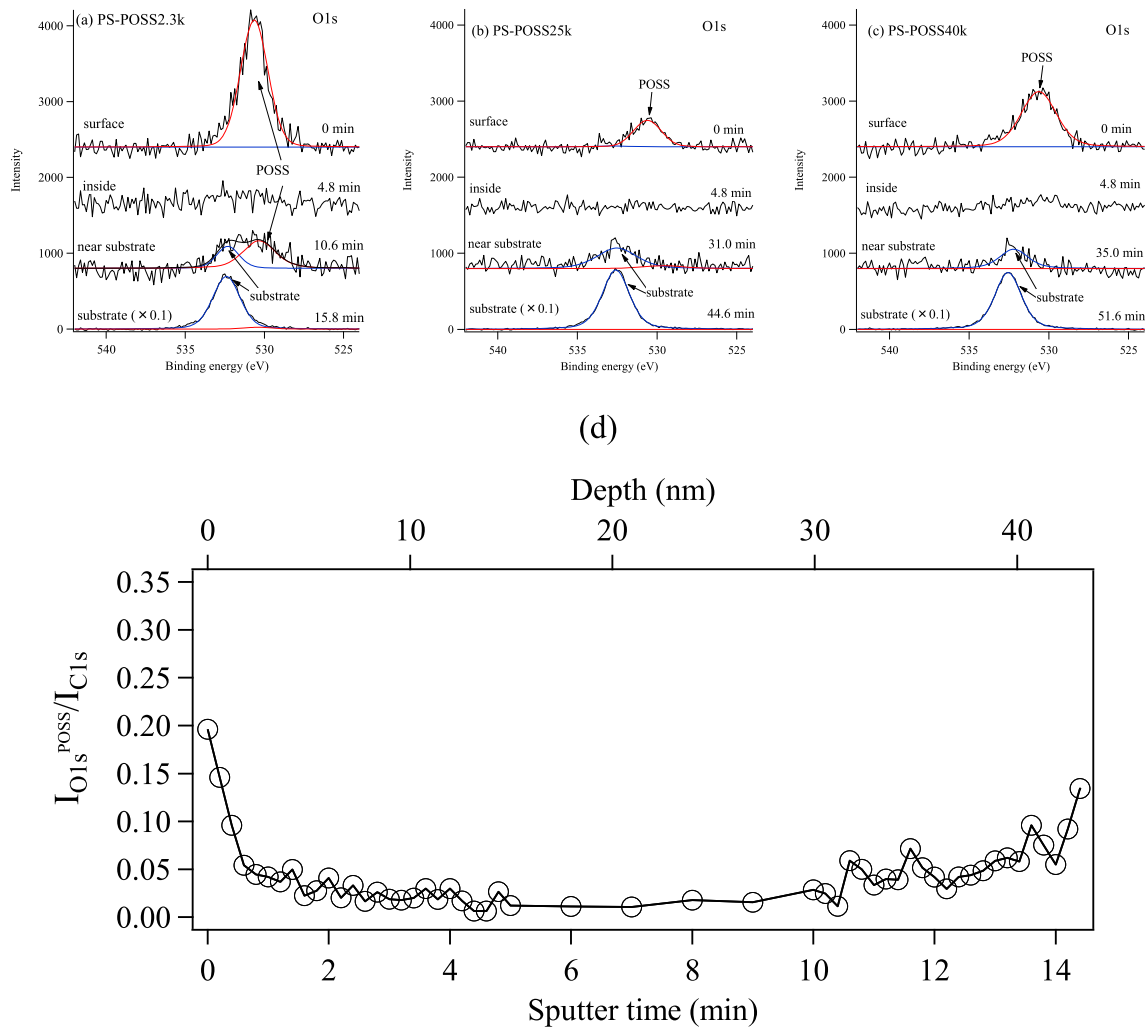


Fig. 4. XPS spectra of O1s near surface of thin films of (a) PS-POSS2.3k, (b) PS-POSS25k and (c) PS-POSS40k sputtered by Ar gas cluster ion beam at various sputter time. Red lines and blue lines are fitting curve for POSS originating peak and substrate originating peak, respectively. (d) Depth profile of the signal ratio of POSS induced O1s to C1s for PS-POSS2.3k. (For interpretation of the references to colour in this figure legend, the reader is referred to the web version of this article.)

the measured $q_{//}$ range of $0.4 < q_{//} < 1.6 \times 10^{-2} \text{ nm}^{-1}$.

Based on hydrodynamic theory and the fluctuation-dissipation theorem [8,9], the $q_{//}$ -dependence of Γ in the overdamped regime on the surface of a uniformly viscous liquid polymer thin film with a nonslip boundary condition underneath is

$$\Gamma = \frac{\gamma}{2\eta} q_{//} \frac{\sinh(q_{//}d) \cosh(q_{//}d) - q_{//}d}{\cosh^2(q_{//}d) + (q_{//}d)^2}, \quad (3a)$$

where d is the film thickness. The solid lines for PS25k and PS-POSS25k in Fig. 7(b) are the dispersion curves calculated from Eq. (3a) with the parameters in Table 2. The experimental data showed good agreement with the calculated lines. For various film thicknesses, Eq. (3a) is rewritten as

$$\Gamma d = \frac{\gamma}{2\eta} (q_{//}d) \frac{\sinh(q_{//}d) \cosh(q_{//}d) - (q_{//}d)}{\cosh^2(q_{//}d) + (q_{//}d)^2}. \quad (3b)$$

In Fig. 7(c), Γd is plotted against $q_{//}d$ for PS25k with thicknesses

of 44, 89, and 155 nm, and PS-POSS25k with thicknesses of 44, 79, and 144 nm, and the theoretical lines calculated from Eq. (3b) are shown. All the measured data for PS25k and PS-POSS25k thin films with different thickness were almost linear, and showed good agreement with the calculated lines. Similar results were obtained for the thin films of PS40k and PS-POSS40k. Experimental Γd for PS40k thin films thicknesses of 50, 81, and 146 nm, and PS-POSS40k thin film thicknesses of 50, 84 and 142 nm, are plotted against $q_{//}d$ in Fig. 8. The result showed good agreement with the theoretical dispersion relation calculated from Eq. (3) with the parameters in Table 2. The GI-XPCS results for PS25k, PS-POSS25k, PS40k, and PS-POSS40k thin films for the PS thin films and the PS-POSS thin films showed similar surface fluctuations. The fluctuations are expressed by the capillary waves on uniformly viscous liquid polymer thin films.

In the spin-coated PS thin films, existence of remaining solvent were reported, and an enrichment of solvent at the Si/PS interfaces were found even if the thin films were annealed [28]. In that case, the lower viscosity layer should be formed at the Si/PS interfaces and the dynamics of capillary waves should become faster and cannot be expressed by only bulk viscosity. However, the present

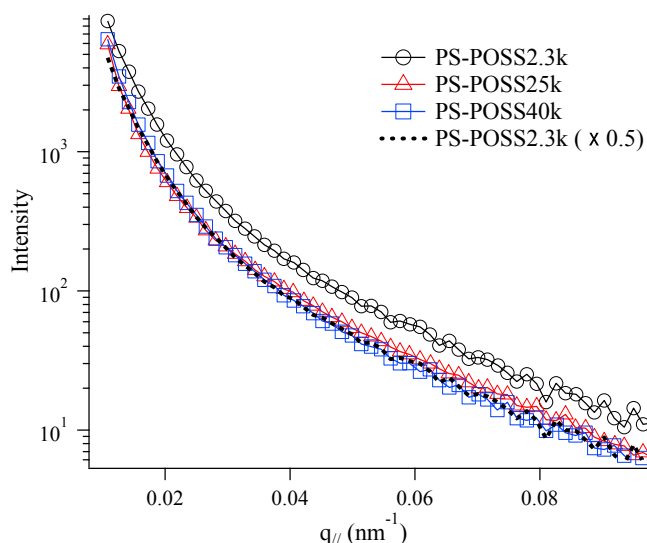


Fig. 5. Scattering intensity profiles of PS-POSS2.3k, PS-POSS25k and PS-POSS40k thin films through grazing incidence small angle scattering (GI-SAXS) measurements. The dashed line is the intensity profile for PS-POSS2.3k multiplied by 0.5.

data were expressed by the capillary waves on uniformly viscous liquid polymer thin films. The remaining solvent effects might be negligible because the content of remaining solvent was very low due to the molecular weight of polymers were relatively small and the long annealing time in the present case.

C. GI-XPCS for low molecular weight PS and PS-POSS thin films ($M_n = 2.3k$)

Fig. 9(a) shows representative data for measured $g_2(q_{||}, t)$ of PS2.3k and PS-POSS2.3k thin films. The $g_2(q_{||}, t)$ values were measured for a 58-nm-thick PS2.5k thin film at $q = 4.74 \times 10^{-3} \text{ nm}^{-1}$ and a 61-nm-thick PS-POSS2.5k thin film at $q_{||} = 4.76 \times 10^{-3} \text{ nm}^{-1}$ at 393 K. Unlike the high molecular weight PS and PS-POSS thin films, $g_2(q_{||}, t)$ for PS-POSS2.3k showed much slower relaxation ($\Gamma = 1.99 \times 10^{-2} \text{ s}^{-1}$, obtained by fitting the data with Eq. (2)) than that for PS2.3k ($\Gamma = 6.20 \times 10^{-1} \text{ s}^{-1}$). The values of Γ obtained from the fitting analysis with Eq. (2) are plotted against $q_{||}$ in Fig. 9(b). Γ for PS-POSS2.3k was much smaller than that for PS2.3k over the entire $q_{||}$ range of our measurements. The solid lines for PS2.3k and PS-POSS2.3k in Fig. 9(b) are the dispersion curves calculated from Eq. (3) with the parameters in Table 3. Although the measured Γ for PS2.3k showed good agreement with the theoretical line (red solid line), the measured Γ for PS-POSS2.3k deviated from the theoretical line (black solid line). In Fig. 9(c) Γd is plotted against $q_{||}d$ for PS2.3k with thicknesses of 47, 58, and 76 nm,

and PS-POSS2.3k with thicknesses of 35, 52, and 61 nm. The theoretical lines calculated from Eq. (3b) using the parameters in Table 3 are also shown. Although the measured Γ for PS2.3k thin films with various thickness were similar and agreed with the theoretical prediction, measured Γ for PS-POSS2.3k were far from the theoretical line. Thus, the observed relaxation behavior for PS-POSS2.3k could not be explained by capillary waves on uniformly viscous liquid polymer thin films.

Based on the study of static structure of low molecular weight PS-POSS thin films, we assumed that the PS-POSS2.3k thin films may not be a uniformly viscous liquid layer, but composed of three different viscous liquid layers. Thus, we explained the measured $q_{||}$ dependence of Γ for PS-POSS2.3k thin films with thicknesses of 35, 53, and 61 nm by considering the capillary waves of thin films composed of three different viscous liquid layers.

The $q_{||}$ dependence of relaxation rate of the capillary waves of liquid surface can be derived from the poles of dynamic susceptibility, which specify the linear response of the surface height to a periodic external force field acting vertically on the liquid surface, by using the classical fluctuation-dissipation theorem. The explicit expression of the dynamic susceptibility for the capillary waves of three layer thin films was derived by extending the bilayer model reported by Jiang et al. [19] and is given in the Appendix.

Fig. 10 shows a three-layer model on a solid substrate where the bottom, middle, and top layers are h_1 , h_2 , and h_3 ($h_3 = d - h_1 - h_2$), respectively. Hereafter, we use subscript and superscript 1, 2 and 3 to denote the bottom (I), center (II), and top layers (III), respectively. For example, the viscosity and the mass density of the bottom layer are denoted η_1 and ρ_1 . The interfacial tension between layers I and II, between II and III, and the surface tension are γ_1 , γ_2 , and γ_3 , respectively. For simplicity, the following assumptions were made: (i) η_2 is same as the bulk viscosity of $1.10 \times 10^3 \text{ Pa s}$; (ii) because the contents of POSS are in the same order as shown in Fig. 4(d), the viscosity of the top layer and the bottom layer are the same ($\eta_1 = \eta_3$); (iii) the difference in the density between the layers is negligible and the densities are same as bulk PS ($\rho_1 = \rho_2 = \rho_3 = 1.0 \text{ g cm}^{-3}$); (iv) because the components of layers are the same materials, $\gamma_1 = \gamma_2 = 0$; and (v) h_1 and h_3 are independent from the total thickness, d , and are fixed.

Applying the three-layer model with the above assumptions to the measured relaxation rates for PS-POSS thin films with thicknesses of 35, 53, and 61 nm produced a set of parameters, $\eta_1 (= \eta_3 = 9.6 \times 10^4 \text{ Pa s})$, h_1 (16 nm), and h_3 (17 nm), which describe the $q_{||}$ dependence of Γ with the minimum residual sum of squares. Fig. 11 shows the calculated relaxation rates from the three-layer model with these parameters. They agreed well with the measured data for all three thin films with different thicknesses. The viscosities of the surface and substrate interface, η_1 and η_3 , were much larger than those in the bulk, meaning that there was a higher viscosity layer at the surface and the substrate interface. This indicates that the molecular motion of PS-POSS was reduced at the

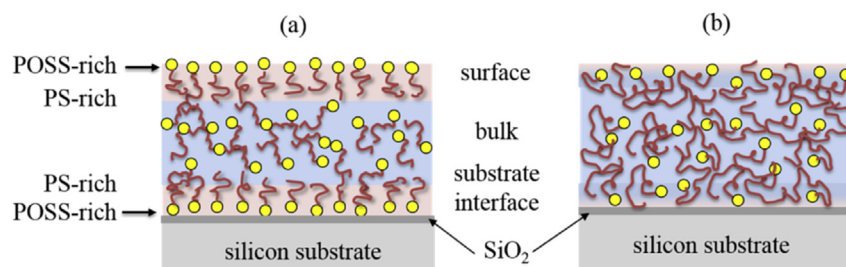


Fig. 6. Schematic drawing of the structure of PS-POSS thin films for low molecular weight (a), and high molecular weight (b).

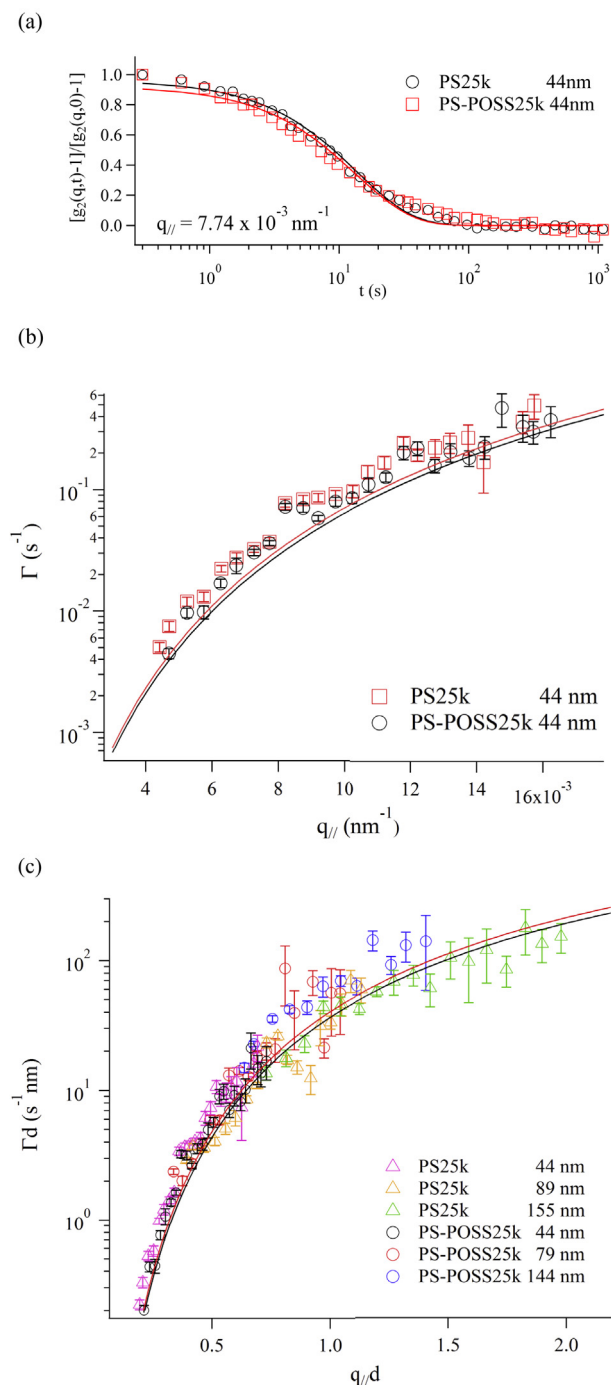


Fig. 7. GI-XPCS results for PS25k and PS-POSS25k thin films at 413 K. (a) Representative results of the measured normalized autocorrelation functions at $q_{||} = 7.74 \times 10^{-3} \text{ nm}^{-1}$ for 44-nm-thick thin films. The solid lines are fitting curves for Eq. (2). (b) $q_{||}$ dependence of Γ obtained from the fitting results of Eq. (2) for 44-nm-thick thin films. The red solid line and the black solid line are calculated from Eq. (3a) for PS25k and PS-POSS25k, respectively, with the values in Table 2. (c) $q_{||}d$ dependence of Γd for various thicknesses of thin films. The red solid line and the black line are calculated from Eq. (3b) for PS25k and PS-POSS25k, respectively, with the values in Table 2. (For interpretation of the references to colour in this figure legend, the reader is referred to the web version of this article.)

top and the bottom layer. Because the dewetting phenomena has been known to have deep correlation with surface fluctuations [29–32], the reduced molecular motion in those layer consequently

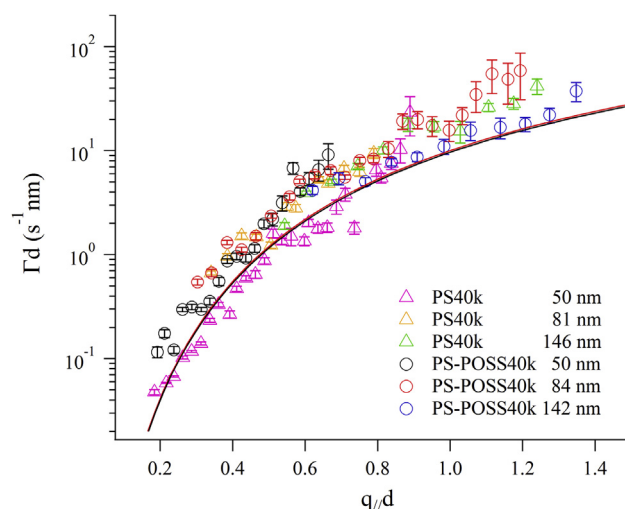


Fig. 8. $q_{||}d$ dependence of Γd for various thicknesses of PS40k and PS-POSS40k thin films. The red solid line and the black line are calculated for PS40k and PS-POSS40k, respectively, from Eq. (3b) with the values in Table 2. (For interpretation of the references to colour in this figure legend, the reader is referred to the web version of this article.)

retarded dewetting behavior, furthermore inhibits the dewetting of PS-POSS thin films in a realistic time window.

The considerable difference of surface dynamics were observed between PS2.3k and PS-POSS2.3k thin films although no major difference was observed between PS and PS-POSS thin films. The origin of these difference should be the large difference of contents, which induced the difference of structure. In the low molecular weight PS-POSS thin films, the layers at surface and substrate interface induced by POSS segregation were relatively robust and strongly affect the surface dynamics. On the other hand, in the high molecular weight PS-POSS thin films, the layers formed by segregation of POSS were weak and thin, thus their effects were weak and negligible.

We will still remain the open question about the deviation of $g_2(q_{||}, t)$ from a single exponential function shown in Figs. 7 and 9(a). Although the deviation from a single exponential function of $g_2(q_{||}, t)$ for polymer thin films has been reported near T_g and high molecular weight, the mechanism has not been clarified yet [33,34]. In the present study, the deviation from a single exponential function were observed for PS-POSS2.3k while that was not observed for PS2.3k thin films. This may indicate that the non-uniform structure of thin films may be the key to solve the question of shape of $g_2(q_{||}, t)$.

4. Conclusion

To investigate the origin of the inhibition of dewetting by POSS functionalization of PS in thin films, we investigated the dynamical behavior of the capillary waves on PS and PS-POSS thin films for molecular weights of 40k, 25k, and 2.3k by GI-XPCS. There was no difference in the dynamics of the capillary waves between the PS and PS-POSS thin films for molecular weights of 40k and 25k. In contrast, for a molecular weight of 2.3k, the dynamics of the PS-POSS thin films were much slower than those of PS thin films. Although the dynamics of the capillary waves of the PS-POSS2.3k thin films were not explained by the uniformly viscous thin film model, they were explained by considering the presence of high-viscosity layers at the surface and the substrate interface.

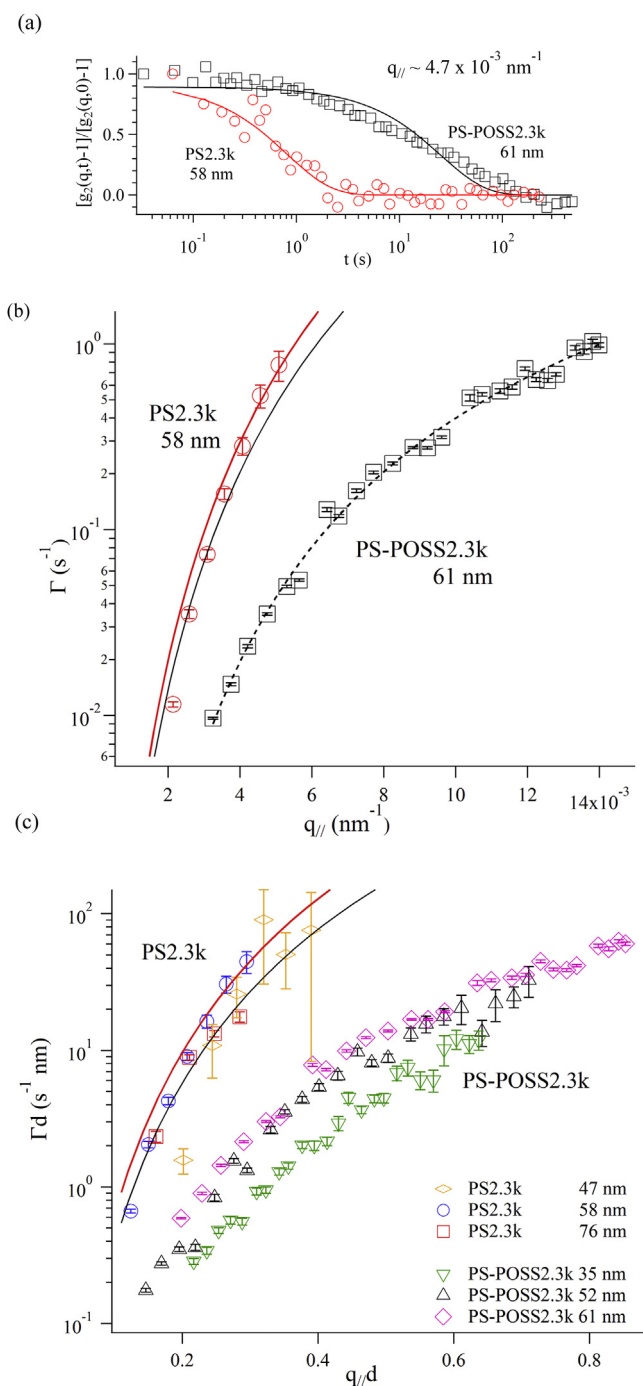


Fig. 9. GI-XPCS results for 58-nm-thick PS2.3k thin film and 61-nm-thick PS-POSS2.3k thin film at 393 K. (a) Representative results of the measured normalized autocorrelation functions for 58-nm-thick PS2.3k thin film at $q_{//} = 4.74 \times 10^{-3} \text{ nm}^{-1}$ and for 61-nm-thick PS-POSS2.3k thin film at $q_{//} = 4.76 \times 10^{-3} \text{ nm}^{-1}$. The solid lines are fitting curves for Eq. (2). (b) $q_{//}$ dependence of Γ obtained from the fitting results of Eq. (2) for 44-nm-thick thin films. The red solid line and the black solid line are calculated from Eq. (3a) for PS2.3k and PS-POSS2.3k, respectively, with the values in Table 3. The black dashed line is a visual guide. (c) $q_{//}d$ dependence of Γd for various thicknesses of thin films. The red solid line and the black line are calculated from Eq. (3b) for PS2.3k and PS-POSS2.3k, respectively, with the values in Table 3. (For interpretation of the references to colour in this figure legend, the reader is referred to the web version of this article.)

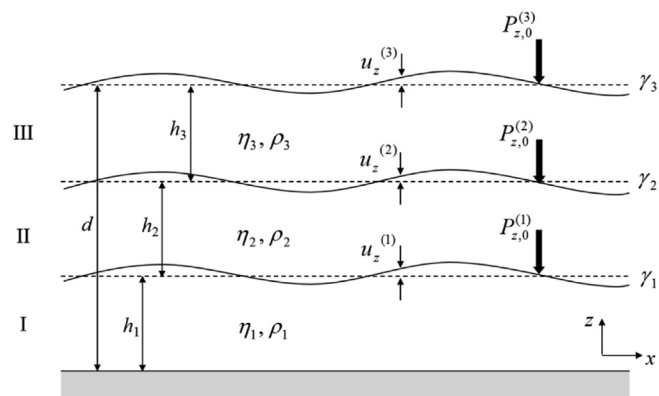


Fig. 10. Geometry and notation of a supported three-layer film. The bottom, center, and top layers are denoted by regions I, II, and III, respectively.

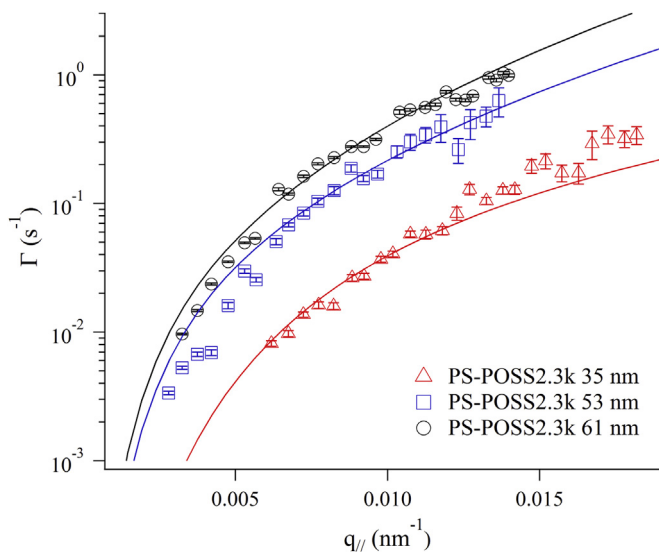


Fig. 11. $q_{//}$ dependence of Γ obtained from the fitting results of Eq. (2) for 35, 53, and 61-nm-thick PS-POSS thin films. The solid lines are derived from the fluctuation-dissipation theorem for three-layer thin films with $\eta_1 = \eta_3 = 9.6 \times 10^4 \text{ Pa s}$, $\eta_2 = 1.10 \times 10^3 \text{ Pa s}$, $d_1 = 16 \text{ nm}$, $d_3 = 17 \text{ nm}$, $\rho_1 = \rho_2 = \rho_3 = 1.0 \text{ g cm}^{-3}$, $\gamma_1 = \gamma_2 = 0$, and $\gamma_3 = 12.8 \text{ mN m}^{-1}$.

Acknowledgement

The authors thank the staff of BL19LXU and BL45XU at Spring-8 for technical support, Dr. S. Narayanan for advice on the GI-XPCS experiments and Dr. T. Nakatani for carrying out part of the GI-SAXS experiments. The GI-XPCS experiments at BL19LXU were performed under the approval of RIKEN (Proposal No. 20130065, 20140079, and 20150069). The GI-SAXS experiments at BL45XU were performed under the approval of RIKEN (Proposal No. 20160057). This work was partially supported by the ImPACT Program of Council for Science, Technology and Innovation (Cabinet Office, Government of Japan). TH acknowledges JSPS Grant-in-Aid for Young Scientists (B) (25790082) and the JST, PRESTO, for funding the project "Molecular technology and creation of new functions."

Appendix. Capillary wave spectra of polymeric three-layer films

The capillary wave spectra of the thermally excited capillary waves on homogeneous supported liquid single-layer films [9] and bilayer films [19] have been studied theoretically. Extending the bilayer model by Jiang et al., the capillary wave spectra of three-layer films and the wave vector dependence of the relaxation rate are derived here.

On a liquid three-layer film on a solid substrate (Fig.10), we assume small periodic externally applied pressure perturbations on the interface and the free surface of the form $P_{z,0}^{(1)} e^{i(kx-\omega t)}$, $P_{z,0}^{(2)} e^{i(kx-\omega t)}$ and $P_{z,0}^{(3)} e^{i(kx-\omega t)}$, with $u_z^{(1)}$, $u_z^{(2)}$ and $u_z^{(3)}$ being the vertical displacements of the reactive fluctuations.

Incompressible liquid is governed by the linearized Navier-Stokes equation

$$\partial_t \mathbf{v} = -\frac{1}{\rho} \nabla p + \nu \nabla^2 \mathbf{v}, \quad (\text{A1})$$

and

$$\text{div} \mathbf{v} = 0 \quad (\text{A2})$$

where \mathbf{v} , p and $\nu = \eta/\rho$ are velocity, pressure, and kinematic viscosity of the liquid, respectively. The solutions of the velocity and pressure in the form of monochromatic plane waves along the x direction are considered,

$$\mathbf{v}^{(j)}(\mathbf{r}, t) = [V_x^{(j)}(z) \mathbf{e}_x + V_z^{(j)}(z) \mathbf{e}_z] e^{i(kx-\omega t)}, \quad (\text{A3a})$$

$$p^{(j)}(\mathbf{r}, t) = P^{(j)}(z) e^{i(kx-\omega t)}, \quad (\text{A3b})$$

where the superscript $j = 1, 2$, and 3 denotes the solutions in regions I, II, and III, respectively. Substituting Eq. (A3a) into (A2), we obtain the expression for velocity amplitudes of

$$ikV_x^{(j)} + \partial_z V_z^{(j)} = 0. \quad (\text{A4})$$

Eq. (A1) leads to the preliminary solutions of the Navier-Stokes equation in regions I, II, and III of

$$V_z^{(j)}(z) = A_k^{(j)} \cosh(kz) + B_k^{(j)} \sinh(kz) + ik\hat{B}_j \cosh(\kappa_j z) + ik\hat{C}_j \sinh(\kappa_j z), \quad (\text{A5a})$$

$$V_x^{(j)}(z) = \frac{i}{k} \partial_z V_z^{(j)}(z), \quad (\text{A5b})$$

where $\kappa_j = \sqrt{k^2 - i\omega/\nu_j}$, and $A_k^{(j)}$, $B_k^{(j)}$, \hat{B}_j , and \hat{C}_j are constants to be determined by the boundary conditions at $z = 0$, h_1 , h_1+h_2 , and d .

(i) Nonslip boundary condition at $z = 0$

The nonslip boundary condition at the substrate interface, $V_x^{(1)}|_{z=0} = V_z^{(1)}|_{z=0} = 0$, gives

$$A_k^{(1)} = -ik\hat{B}_k^{(1)}, \quad B_k^{(1)} = -ik_1\hat{C}_1. \quad (\text{A6})$$

The xz and zz components of the stress tensor in regions I, II, and III are denoted as

$$\sigma_{xz}^{(j)} \equiv \hat{\sigma}_{xz}^{(j)} e^{i(kx-\omega t)} = \eta_j (\partial_z v_x^{(j)} + \partial_x v_z^{(j)}), \quad (\text{A7a})$$

$$\sigma_{zz}^{(j)} \equiv \hat{\sigma}_{zz}^{(j)} e^{i(kx-\omega t)} = -p^{(j)} + 2\eta_j \partial_z v_z^{(j)}. \quad (\text{A7b})$$

Then Eqs. (A5), (A6) and (A7a) can be combined into compact matrix expressions as

$$\mathbf{X} = \mathbf{BZ}, \text{ region I}, \quad (\text{A8a})$$

$$\mathbf{W} = \mathbf{AY}, \text{ region II}, \quad (\text{A8b})$$

$$\mathbf{R} = \mathbf{LS}, \text{ region III}, \quad (\text{A8c})$$

where \mathbf{X} and \mathbf{Z} , \mathbf{W} , and \mathbf{Y} , \mathbf{R} and \mathbf{L} are defined for regions I, II, and III, respectively, as

$$\mathbf{X} = \begin{bmatrix} V_x^{(1)} \\ V_z^{(1)} \\ P^{(1)}/\rho_1 \\ \hat{\sigma}_{xz}^{(1)} \end{bmatrix}, \quad \mathbf{Z} = \begin{bmatrix} \hat{B}_1 \\ \hat{C}_1 \end{bmatrix}, \quad (\text{A9a})$$

$$\mathbf{W} = \begin{bmatrix} V_x^{(2)} \\ V_z^{(2)} \\ P^{(2)}/\rho_2 \\ \hat{\sigma}_{xz}^{(2)} \end{bmatrix}, \quad \mathbf{Y} = \begin{bmatrix} A_k^{(2)} \\ B_k^{(2)} \\ \hat{B}_2 \\ \hat{C}_2 \end{bmatrix}, \quad (\text{A9b})$$

$$\mathbf{R} = \begin{bmatrix} V_x^{(3)} \\ V_z^{(3)} \\ P^{(3)}/\rho_3 \\ \hat{\sigma}_{xz}^{(3)} \end{bmatrix}, \quad \mathbf{S} = \begin{bmatrix} A_k^{(3)} \\ B_k^{(3)} \\ \hat{B}_3 \\ \hat{C}_3 \end{bmatrix}, \quad (\text{A9c})$$

and the matrices \mathbf{B} , \mathbf{A} , and \mathbf{L} are defined as

$$\mathbf{B} = \begin{bmatrix} k \sinh(kz) - \kappa_1 \sinh(\kappa_1 z) & \kappa_1 \cosh(kz) - \kappa_1 \cosh(\kappa_1 z) \\ -ik \cosh(kz) + ik \cosh(\kappa_1 z) & -ik_1 \sinh(kz) + ik \sinh(\kappa_1 z) \\ \omega \sinh(kz) & \omega(\kappa_1/k) \cosh(kz) \\ 2\eta_1 k^2 \cosh(kz) - \eta_1 (k^2 + \kappa_1^2) \cosh(\kappa_1 z) & 2\eta_1 k \kappa_1 \sinh(kz) - \eta_1 (k^2 + \kappa_1^2) \sinh(\kappa_1 z) \end{bmatrix}, \quad (\text{A10a})$$

$$\frac{P^{(j)}(z)}{\rho_j} = \frac{i\nu_j}{k} (\kappa_j^2 - \partial_z^2) V_x^{(j)}(z), \quad (\text{A5c})$$

$$\mathbf{A} = \begin{bmatrix} i \sinh(kz) & i \cosh(kz) & -\kappa_2 \sinh(\kappa_2 z) & -\kappa_2 \cosh(\kappa_2 z) \\ \cosh(kz) & \sinh(kz) & ik \cosh(\kappa_2 z) & ik \sinh(\kappa_2 z) \\ (i\omega/k)\sinh(kz) & (i\omega/k)\cosh(kz) & 0 & 0 \\ 2ik\eta_2 \cosh(kz) & 2ik\eta_2 \sinh(kz) & -\eta_2(k^2 + \kappa_2^2)\cosh(\kappa_2 z) & -\eta_2(k^2 + \kappa_2^2)\sinh(\kappa_2 z) \end{bmatrix}, \quad (\text{A10b})$$

$$\mathbf{L} = \begin{bmatrix} i \sinh(kz) & i \cosh(kz) & -\kappa_3 \sinh(\kappa_3 z) & -\kappa_3 \cosh(\kappa_3 z) \\ \cosh(kz) & \sinh(kz) & ik \cosh(\kappa_3 z) & ik \sinh(\kappa_3 z) \\ (i\omega/k)\sinh(kz) & (i\omega/k)\cosh(kz) & 0 & 0 \\ 2ik\eta_3 \cosh(kz) & 2ik\eta_3 \sinh(kz) & -\eta_3(k^2 + \kappa_3^2)\cosh(\kappa_3 z) & -\eta_3(k^2 + \kappa_3^2)\sinh(\kappa_3 z) \end{bmatrix}, \quad (\text{A10c})$$

The hydrodynamic problem reduces to the problem of solving for coefficients \mathbf{Z} , \mathbf{Y} , and \mathbf{S} via the three boundary conditions at $z=h_1$, h_1+h_2 , and d .

ii) Interfacial boundary condition at $z = h_1$

The boundary condition of the equal velocities of the liquid on both sides at the interface gives

$$V_x^{(2)} = V_x^{(1)}, \quad V_z^{(2)} = V_z^{(1)}, \quad (\text{A11a})$$

and the equilibrium of force at the interface gives

$$\hat{\sigma}_{xz}^{(2)} = \hat{\sigma}_{xz}^{(1)}, \quad (\text{A11b})$$

$$\hat{\sigma}_{zz}^{(2)} - \hat{\sigma}_{zz}^{(1)} = [\gamma_1 k^2 + g(\rho_1 - \rho_2)] U_z^{(1)} - P_{z,0}^{(1)}, \quad (\text{A11c})$$

where $U_z^{(1)}$ is the amplitude of the vertical displacement of interfacial fluctuations expressed by $u_z^{(1)} = U_z^{(1)} e^{i(kx - \omega t)}$. Using Eqs. (A4) and (A7b) and relation $u_z^{(1)} = \frac{i}{\omega} v_z^{(1)} \Big|_{z=h_1}$, derived from $v_z^{(1)} \Big|_{z=h_1} = \partial_t u_z^{(1)}$, Eq. (A11) can be rewritten as

$$\mathbf{W}|_{z=h_1} = \mathbf{TX}|_{z=h_1} + \mathbf{U}, \quad (\text{A12})$$

where

$$\mathbf{U} = \begin{bmatrix} 0 \\ 0 \\ P_{z,0}^{(1)}/\rho_2 \\ 0 \end{bmatrix}, \quad (\text{A13a})$$

$$\mathbf{T} = \begin{bmatrix} 1 & 0 & 0 & 0 \\ 0 & 1 & 0 & 0 \\ \frac{2ik(\eta_1 - \eta_2)}{\rho_2} & \frac{i(\gamma_1 k^2 + g(\rho_1 - \rho_2))}{\rho_2 \omega} & \frac{\rho_1}{\rho_2} & 0 \\ 0 & 0 & 0 & 1 \end{bmatrix}. \quad (\text{A13b})$$

Combining Eqs. (A8) and (A12), \mathbf{Y} (for region II) and \mathbf{Z} (for region I) can be related as

$$\begin{aligned} \mathbf{Y} &= \mathbf{A}^{-1} \mathbf{W}|_{z=h_1} = \mathbf{A}^{-1} \mathbf{TX}|_{z=h_1} + \mathbf{A}^{-1} \mathbf{U}|_{z=h_1} \\ &= \mathbf{A}^{-1} \mathbf{TBZ}|_{z=h_1} + \mathbf{A}^{-1} \begin{bmatrix} 0 \\ 0 \\ P_{z,0}^{(1)}/\rho_2 \\ 0 \end{bmatrix} \Big|_{z=h_1}, \end{aligned} \quad (\text{A14a})$$

$$Y_k = \sum_{l=1}^2 C_{kl} Z_l + \frac{P_{z,0}^{(1)}}{\rho_2} A_{k3}^{-1} \Big|_{z=h_1}, \quad (\text{A14b})$$

where the intermediate matrix \mathbf{C} is given by

$$\mathbf{C} = (\mathbf{A}^{-1} \mathbf{TB}) \Big|_{z=h_1} \quad (\text{A14c})$$

iii) Interfacial boundary condition at $z = h_1 + h_2$

The boundary condition at $z = h_1 + h_2$ are given in the same manner as $z = h_1$. The following equations are obtained at $z = h_1 + h_2$,

$$V_x^{(3)} = V_x^{(2)}, \quad V_z^{(3)} = V_z^{(2)}, \quad (\text{A15a})$$

$$\hat{\sigma}_{xz}^{(3)} = \hat{\sigma}_{xz}^{(2)}, \quad (\text{A15b})$$

$$\hat{\sigma}_{zz}^{(3)} - \hat{\sigma}_{zz}^{(2)} = [\gamma_2 k^2 + g(\rho_2 - \rho_3)] U_z^{(2)} - P_{z,0}^{(2)}. \quad (\text{A15c})$$

Eqs. (A15a)–(A15c) are summarized as

$$\mathbf{R}|_{z=h_1+h_2} = \mathbf{KW}|_{z=h_1+h_2} + \mathbf{J}, \quad (\text{A16a})$$

where

$$\mathbf{J} = \begin{bmatrix} 0 \\ 0 \\ P_{z,0}^{(2)}/\rho_3 \\ 0 \end{bmatrix}, \quad (\text{A16b})$$

$$\mathbf{K} = \begin{bmatrix} 1 & 0 & 0 & 0 \\ 0 & 1 & 0 & 0 \\ \frac{2ik(\eta_2 - \eta_3)}{\rho_3} & \frac{i(\gamma_2 k^2 + g(\rho_2 - \rho_3))}{\rho_3 \omega} & \frac{\rho_2}{\rho_3} & 0 \\ 0 & 0 & 0 & 1 \end{bmatrix}. \quad (\text{A16c})$$

Combining Eqs. (A8) and (A16), \mathbf{S} (for region III) and \mathbf{Y} (for region II) can be related,

$$\begin{aligned} \mathbf{S} &= \mathbf{L}^{-1} \mathbf{R}|_{z=h_1+h_2} = \mathbf{L}^{-1} \mathbf{K} \mathbf{W}|_{z=h_1+h_2} + \mathbf{L}^{-1} \mathbf{J}|_{z=h_1+h_2} \\ &= \mathbf{L}^{-1} \mathbf{K} \mathbf{A} \mathbf{Y}|_{z=h_1+h_2} + \mathbf{L}^{-1} \begin{bmatrix} 0 \\ 0 \\ P_{z,0}^{(2)}/\rho_3 \\ 0 \end{bmatrix} \Big|_{z=h_1+h_2}, \end{aligned} \quad (\text{A17a})$$

$$S_k = \sum_{l=1}^2 F_{kl} Y_l + \frac{P_{z,0}^{(2)}}{\rho_3} L_{k3}^{-1} \Big|_{z=h_1+h_2}, \quad (\text{A17b})$$

where

$$\mathbf{F} = (\mathbf{L}^{-1} \mathbf{K} \mathbf{A}) \Big|_{z=h_1+h_2}. \quad (\text{A17c})$$

iv) Surface boundary condition at $z = d$

The boundary condition at the free surface gives

$$\hat{\sigma}_{xz}^{(3)} = \eta_3 (\partial_z V_x^{(3)} + ik V_z^{(3)}) = 0, \quad (\text{A18a})$$

$$\hat{\sigma}_{zz}^{(3)} = -P^{(3)} + 2\eta_3 \partial_z V_z^{(3)} = -(\gamma_3 k^2 + g\rho_3) U_z^{(3)} + P_{z,0}^{(3)}. \quad (\text{A18b})$$

From the equation of continuity Eq. (A4), Eq. (A18a) can be rewritten as

$$\mathbf{D} \mathbf{S} = 0, \quad (\text{A19a})$$

where

$$\mathbf{D} = \begin{bmatrix} 2k \cosh(kd) \\ 2k \sinh(kd) \\ i(k^2 + \kappa_3^2) \cosh(\kappa_3 d) \\ i(k^2 + \kappa_3^2) \sinh(\kappa_3 d) \end{bmatrix}^T. \quad (\text{A19b})$$

Applying the vertical surface displacement $u_z^{(3)} = \frac{i}{\omega} v_z^{(3)} \Big|_{z=d}$ to Eq. (A18b) gives the expression

$$\mathbf{E} \mathbf{S} = \frac{P_{z,0}^{(3)}}{\rho_3}, \quad (\text{A20a})$$

where

$$\mathbf{E} = \begin{bmatrix} \left(2\nu_3 k - \frac{i\omega}{k}\right) \sinh(kd) + \frac{i(\gamma_3 k^2 + g\rho_3)}{\rho_3 \omega} \cosh(kd) \\ \left(2\nu_3 k - \frac{i\omega}{k}\right) \cosh(kd) + \frac{i(\gamma_3 k^2 + g\rho_3)}{\rho_3 \omega} \sinh(kd) \\ 2i\nu_3 k \kappa_3 \sinh(\kappa_3 d) - \frac{k(\gamma_3 k^2 + g\rho_3)}{\rho_3 \omega} \cosh(\kappa_3 d) \\ 2i\nu_3 k \kappa_3 \cosh(\kappa_3 d) - \frac{k(\gamma_3 k^2 + g\rho_3)}{\rho_3 \omega} \sinh(\kappa_3 d) \end{bmatrix}^T. \quad (\text{A20b})$$

Combining Eqs. (A19a), (A14) and (A17) gives the expressions

$$\begin{aligned} \mathbf{D} \mathbf{S} &= \mathbf{D} \left(\mathbf{F} \mathbf{Y} + \mathbf{L}^{-1} \begin{bmatrix} 0 \\ 0 \\ P_{z,0}^{(2)}/\rho_3 \\ 0 \end{bmatrix} \Big|_{z=h_1+h_2} \right) \\ &= \mathbf{D} \left(\mathbf{F} \left(\mathbf{C} \mathbf{Z} + \mathbf{A}^{-1} \begin{bmatrix} 0 \\ 0 \\ P_{z,0}^{(1)}/\rho_2 \\ 0 \end{bmatrix} \Big|_{z=h_1} \right) \right. \\ &\quad \left. + \mathbf{D} \mathbf{L}^{-1} \begin{bmatrix} 0 \\ 0 \\ P_{z,0}^{(2)}/\rho_3 \\ 0 \end{bmatrix} \Big|_{z=h_1+h_2} \right) \\ &= 0, \end{aligned} \quad (\text{A21a})$$

$$\sum_{l=1}^2 P_l Z_l = -\frac{P_{z,0}^{(1)}}{\rho_2} P_0^{h_1} - \frac{P_{z,0}^{(2)}}{\rho_3} P_0^{h_1+h_2}, \quad (\text{A21b})$$

where

$$P_l = (\mathbf{D} \mathbf{F} \mathbf{C})_l, \quad P_0^{h_1} = (\mathbf{D} \mathbf{F} \mathbf{A}^{-1})_3 \Big|_{z=h_1} P_0^{h_1+h_2} = (\mathbf{D} \mathbf{L}^{-1})_3 \Big|_{z=h_1+h_2}. \quad (\text{A21c})$$

Combining Eqs. (A19b), (A14) and (A17) gives the expressions

$$\begin{aligned} \mathbf{E} \mathbf{S} &= \mathbf{E} \left(\mathbf{F} \mathbf{Y} + \mathbf{L}^{-1} \begin{bmatrix} 0 \\ 0 \\ P_{z,0}^{(2)}/\rho_3 \\ 0 \end{bmatrix} \Big|_{z=h_1+h_2} \right) \\ &= \mathbf{E} \left(\mathbf{F} \left(\mathbf{C} \mathbf{Z} + \mathbf{A}^{-1} \begin{bmatrix} 0 \\ 0 \\ P_{z,0}^{(1)}/\rho_2 \\ 0 \end{bmatrix} \Big|_{z=h_1} \right) \right. \\ &\quad \left. + \mathbf{L}^{-1} \begin{bmatrix} 0 \\ 0 \\ P_{z,0}^{(2)}/\rho_3 \\ 0 \end{bmatrix} \Big|_{z=h_1+h_2} \right) \\ &= \frac{P_{z,0}^{(3)}}{\rho_3}, \end{aligned} \quad (\text{A22a})$$

$$\sum_{l=1}^2 Q_l Z_l = -\frac{P_{z,0}^{(3)}}{\rho_2} Q_0^{h_1} - \frac{P_{z,0}^{(2)}}{\rho_3} Q_0^{h_1+h_2}, \quad (\text{A22b})$$

where

$$Q_l = (\mathbf{EFC})_l, \quad Q_0^{h_1} = (\mathbf{EFA}^{-1})_3|_{z=h_1}, \quad Q_0^{h_1+h_2} = (\mathbf{EL}^{-1})_3|_{z=h_1+h_2}. \quad (\text{A22c})$$

v) Surface and interfacial dynamic susceptibilities

Solving Eqs. (A21b) and (A22b) for \mathbf{Z} gives the expressions

$$[\mathbf{M}, \mathbf{P}, \mathbf{Q}] = \sum_{i,j,k=0}^2 \varepsilon_{ijk} M_i P_j Q_k, \quad (\text{A25b})$$

ε_{ijk} is the Levi-Civita symbol, and

$$\mathbf{G} = \begin{bmatrix} \cosh(k(h_1 + h_2)) \\ \sinh(k(h_1 + h_2)) \\ ik \cosh(\kappa_2(h_1 + h_2)) \\ ik \sinh(\kappa_2(h_1 + h_2)) \end{bmatrix}^T. \quad (\text{A25b})$$

$$Z_1 = \frac{(P_2 Q_0^{h_1} - P_0^{h_1} Q_2) (P_{z,0}^{(1)} / \rho_2) + (P_2 Q_0^{h_1+h_2} - P_0^{h_1+h_2} Q_2) (P_{z,0}^{(2)} / \rho_3) - P_2 (P_{z,0}^{(3)} / \rho_3)}{P_1 Q_2 - P_2 Q_1}, \quad (\text{A23a})$$

$$Z_2 = \frac{(P_0^{h_1} Q_1 - P_1 Q_0^{h_1}) (P_{z,0}^{(1)} / \rho_2) + (P_0^{h_1+h_2} Q_1 - P_1 Q_0^{h_1+h_2}) (P_{z,0}^{(2)} / \rho_3) - P_1 (P_{z,0}^{(3)} / \rho_3)}{P_1 Q_2 - P_2 Q_1}. \quad (\text{A23b})$$

Then, the monochromatic plane-wave solutions can be obtained. The amplitudes of vertical interfacial fluctuation between region I and II is given by

$$U_z^{(1)} = \frac{i}{\omega} V_z^{(1)}|_{z=h_1} = \frac{i}{\omega} \sum_{k=1}^2 N_k Z_k \\ = \frac{i}{\omega} \frac{1}{[\mathbf{P}, \mathbf{Q}]} \left[\frac{P_0^{h_1} [\mathbf{Q}, \mathbf{N}] - Q_0^{h_1} [\mathbf{P}, \mathbf{N}]}{\rho_2} P_{z,0}^{(1)} + \frac{[\mathbf{P}, \mathbf{N}]}{\rho_2} P_{z,0}^{(2)} \right], \quad (\text{A24a})$$

where

$$[\mathbf{P}, \mathbf{Q}] \equiv P_1 Q_2 - P_2 Q_1, \quad (\text{A24b})$$

$$\mathbf{N} = \begin{bmatrix} -i[k \cosh(kh_1) - k \cosh(\kappa_1 h_1)] \\ -i[\kappa_1 \sinh(kh_1) - k \sinh(\kappa_1 h_1)] \end{bmatrix}^T. \quad (\text{A24c})$$

Referring to Eq. (A14), the amplitudes of vertical interfacial fluctuation between regions II and III is given as

$$U_z^{(2)} = \frac{i}{\omega} V_z^{(2)}|_{z=h_1+h_2} = \frac{i}{\omega} \sum_{k=1}^4 G_k Y_k \\ = \frac{i}{\omega} \frac{1}{[\mathbf{P}, \mathbf{Q}]} \left[\frac{[\mathbf{M}, \mathbf{P}, \mathbf{Q}]}{\rho_2} P_{z,0}^{(1)} \right. \\ \left. + \frac{(P_2 Q_0^{h_1+h_2} - P_0^{h_1+h_2} Q_2) M_1 + (P_0^{h_1+h_2} Q_1 - P_1 Q_0^{h_1+h_2}) M_2}{\rho_3} P_{z,0}^{(2)} \right. \\ \left. - \frac{[\mathbf{P}, \mathbf{M}]}{\rho_3} P_{z,0}^{(3)} \right] \quad (\text{A25a})$$

where

Referring to Eq. (A17), the amplitudes of vertical surface fluctuation is given as

$$U_z^{(3)} = \frac{i}{\omega} V_z^{(3)}|_{z=d} = \frac{i}{\omega} \sum_{k=1}^4 H_k S_k \\ = \frac{i}{\omega} \frac{1}{[\mathbf{P}, \mathbf{Q}]} \left[\left\{ \Theta_1 (P_2 Q_0^{h_1} - P_0^{h_1} Q_2) + \Theta_2 (P_0^{h_1} Q_1 - P_1 Q_0^{h_1}) \right. \right. \\ \left. \left. + A_3 [\mathbf{P}, \mathbf{Q}] \right\} \frac{P_{z,0}^{(1)}}{\rho_2} + \left\{ \Theta_1 (P_2 Q_0^{h_1+h_2} - P_0^{h_1+h_2} Q_2) \right. \right. \\ \left. \left. + \Theta_2 (P_0^{h_1+h_2} Q_1 - P_1 Q_0^{h_1+h_2}) + Q_3 [\mathbf{P}, \mathbf{Q}] \right\} \frac{P_{z,0}^{(2)}}{\rho_3} + \{ -\Theta_1 P_2 \right. \\ \left. + \Theta_2 P_1 \} \frac{P_{z,0}^{(3)}}{\rho_3} \right] \quad (\text{A26a})$$

$$\mathbf{H} = \begin{bmatrix} \cosh(kd) \\ \sinh(kd) \\ ik \cosh(\kappa_3 d) \\ ik \sinh(\kappa_3 d) \end{bmatrix}^T \quad (\text{A26b})$$

$$\mathbf{S} = \mathbf{FCZ} + \mathbf{FA}^{-1} \begin{bmatrix} 0 \\ 0 \\ P_{z,0}^{(1)} / \rho_2 \\ 0 \end{bmatrix} \Big|_{z=h_1} + \mathbf{L}^{-1} \begin{bmatrix} 0 \\ 0 \\ P_{z,0}^{(2)} / \rho_3 \\ 0 \end{bmatrix} \Big|_{z=h_1+h_2} \quad (\text{A26c})$$

Eqs. (A24a), (A25a) and (A26a) can be rewritten as $U_z^{(i)} = \sum_j \chi_{zz}^{(ij)} P_{z,0}^{(j)}$. Thus, the self- and cross-dynamic susceptibilities for the interface and the free surface are obtained via the linear response theory are

$$\chi_{zz} = \frac{i}{\omega} \frac{1}{[\mathbf{P}, \mathbf{Q}]} \Xi \quad (\text{A27a})$$

$$\Xi_{11} = \frac{P_0^{h_1} [\mathbf{Q}, \mathbf{N}] - Q_0^{h_1} [\mathbf{P}, \mathbf{N}]}{\rho_2}, \quad \Xi_{12} = \frac{[\mathbf{P}, \mathbf{N}]}{\rho_2}, \quad \Xi_{13} = 0$$

$$\Xi_{21} = \frac{[\mathbf{M}, \mathbf{P}, \mathbf{Q}]}{\rho_2}, \quad \Xi_{22} = \frac{(P_2 Q_0^{h_1+h_2} - P_0^{h_1+h_2} Q_2) M_1 + (P_0^{h_1+h_2} Q_1 - P_1 Q_0^{h_1+h_2}) M_2}{\rho_3}$$

$$\Xi_{23} = -\frac{[\mathbf{P}, \mathbf{M}]}{\rho_3}$$

$$\Xi_{31} = \frac{\Theta_1 (P_2 Q_0^{h_1} - P_0^{h_1} Q_2) + \Theta_2 (P_0^{h_1} Q_1 - P_1 Q_0^{h_1}) + \Lambda_3 [P, Q]}{\rho_2}$$

$$\Xi_{32} = \frac{\Theta_1 (P_2 Q_0^{h_1+h_2} - P_0^{h_1+h_2} Q_2) + \Theta_2 (P_0^{h_1+h_2} Q_1 - P_1 Q_0^{h_1+h_2}) + \Omega_3 [P, Q]}{\rho_3}$$

$$\Xi_{33} = \frac{-\Theta_1 P_2 + \Theta_2 P_1}{\rho_3} \quad (\text{A27b})$$

According to the fluctuation-dissipation theorem, the power spectrum of thermal height fluctuations of the interface and the free surface is given by

$$S_{zz}^{(ij)}(k, \omega) = \int dt \langle u_z^{(i)}(k, t) u_z^{(j)}(-k, 0) \rangle e^{i\omega t} = 2k_B T \frac{\text{Im}[\chi_{zz}^{(ij)}(k, \omega)]}{\omega} \quad (\text{A28})$$

The frequencies and damping rates can be obtained by the poles of $\chi_{zz}^{(ij)}(k, \omega)$ in the lower half of the complex ω plane. For highly viscous polymeric liquids, propagating modes are usually suppressed, and only overdamped modes exist. The Fourier transform of the surface or interfacial fluctuation spectrum in the time domain is given as the sum of the overdamped modes at these poles as

$$S_{zz}^{(ij)}(k, t) = S_{zz}^{(ij)}(k) \sum_m a_m(k) e^{-\Gamma_m(k)t}, \quad (\text{A29})$$

where $S_{zz}^{(ij)}(k) = k_B T \chi_{zz}^{(ij)}(k, 0)$ is the total power of the spectrum and a_m is the mode amplitude,

$$a_m(k) = \frac{\text{Res}[\chi_{zz}^{(ij)}(k, -i\Gamma_m)]}{\chi_{zz}^{(ij)}(k, 0) \Gamma_m} \quad (\text{A30})$$

with the total amplitudes $\sum_m a_m(k) = 1$.

The relaxation rates of free surface fluctuations of three layer thin films are numerically obtained by looking for the poles of $\chi_{zz}^{(33)}(k, \omega)$.

References

- [1] P. Muller-Buschbaum, J. Physics-Condensed Matter 15 (36) (2003) R1549–R1582.
- [2] M. Rauscher, S. Dietrich, Annu. Rev. Mater. Res. 38 (1) (2008) 143–172.
- [3] L. Xue, Y. Han, Prog. Polym. Sci. 36 (2) (2011) 269–293.
- [4] L. Xue, Y. Han, Prog. Mater. Sci. 57 (6) (2012) 947–979.
- [5] N. Hosaka, N. Torikai, H. Otsuka, A. Takahara, Langmuir 23 (2) (2007) 902–907.
- [6] N. Hosaka, H. Otsuka, M. Hino, A. Takahara, Langmuir 24 (11) (2008) 5766–5772.
- [7] K. Miyamoto, N. Hosaka, M. Kobayashi, H. Otsuka, N. Yamada, N. Torikai, A. Takahara, Polym. J. 39 (12) (2007) 1247–1252.
- [8] J.L. Harden, H. Pleiner, P.A. Pincus, J. Chem. Phys. 94 (7) (1991) 5208.
- [9] J. Jackle, J. Physics-Condensed Matter 10 (32) (1998) 7121–7131.
- [10] D. Langevin, Light Scattering by Liquid Surfaces and Complementary Techniques, M. Dekker, New York, 1992.
- [11] T. Hoshino, Y. Ohmasa, R. Osada, M. Yao, Physical Review E 78 (6) (2008).
- [12] H. Kim, A. Rühm, L.B. Lurio, J.K. Basu, J. Lal, D. Lumma, S.G.J. Mochrie, S.K. Sinha, Phys. Rev. Lett. 90 (6) (2003).
- [13] A. Madsen, T. Seydel, M. Sprung, C. Gutt, M. Tolan, G. Grubel, Phys. Rev. Lett. 92 (9) (2004) 096104.
- [14] Z. Jiang, H. Kim, X. Jiao, H. Lee, Y.J. Lee, Y. Byun, S. Song, D. Eom, C. Li, M.H. Rafailovich, L.B. Lurio, S.K. Sinha, Phys. Rev. Lett. 98 (22) (2007).
- [15] B. Akgun, Ugur Gke, Z. Jiang, S. Narayanan, S. Song, H. Lee, W.J. Brittain, H. Kim, S.K. Sinha, M.D. Foster, Macromolecules 42 (3) (2009) 737–741.
- [16] Wang S-f, S. Yang, J. Lee, B. Akgun, D.T. Wu, M.D. Foster, Phys. Rev. Lett. 111 (6) (2013).
- [17] S.K. Sinha, Z. Jiang, L.B. Lurio, Adv. Mater. 26 (46) (2014) 7764–7785.
- [18] H. Lee, X. Li, H. Kim, Z. Jiang, J.-R. Lim, J. Lee, J. Korean Phys. Soc. 57 (6) (2010) 1412.
- [19] Z. Jiang, H. Kim, S.G.J. Mochrie, L.B. Lurio, S.K. Sinha, Phys. Rev. E 74 (1) (2006).
- [20] M. Yabashi, T. Mochizuki, H. Yamazaki, S. Goto, H. Ohashi, K. Takeshita, T. Ohata, T. Matsushita, K. Tamasaku, Y. Tanaka, T. Ishikawa, Nuclear Instruments & Methods in Physics Research Section a-Accelerators Spectrometers Detectors and Associated Equipment, vol. 467, 2001, pp. 678–681.
- [21] T. Hoshino, M. Kikuchi, D. Murakami, Y. Harada, K. Mitamura, K. Ito, Y. Tanaka, S. Sasaki, M. Takata, H. Jinnai, A.J. Takahara, Synchrotron Radiat. 19 (Pt 6) (2012) 988–993.
- [22] T. Hoshino, D. Murakami, K. Ito, Y. Tanaka, S. Sasaki, M. Takata, H. Jinnai, A. Takahara, Polym. J. 45 (1) (2012) 94–99.
- [23] T. Hoshino, D. Murakami, Y. Tanaka, M. Takata, H. Jinnai, A. Takahara, Phys. Rev. E Stat. Nonlin Soft Matter Phys. 88 (2013) 032602.
- [24] M. Tariq, A.P. Serro, J.L. Mata, B. Saramago, J.M.S.S. Esperança, J.N. Canongia Lopes, L.P.N. Rebelo, Fluid Phase Equilibria 294 (1–2) (2010) 131–138.
- [25] T. Miyayama, N. Sanada, M. Suzuki, J.S. Hammond, S.Q.D. Si, A. Takahara, J. Vac. Sci. Technol. A Vac. Surfaces, Films 28 (2) (2010) L1.
- [26] Y. Yamamoto, K. Ichiki, T. Seki, T. Aoki, J. Matsuo, Surf. Interface Analysis 45 (1) (2013) 167–170.
- [27] T. Fujisawa, K. Inoue, T. Oka, H. Iwamoto, T. Uruga, T. Kumasaka, Y. Inoko, N. Yagi, M. Yamamoto, T. Ueki, J. Appl. Crystallogr. 33 (1) (2000) 797–800.
- [28] J. Perlich, V. Korstgens, E. Metwalli, L. Schulz, R. Georgii, P. Muller-Buschbaum, Macromolecules 42 (1) (2009) 337–344.
- [29] A. Vrij, J.T. Overbeek, J. Am. Chem. Soc. 90 (12) (1968), 3074–+.
- [30] F.B. Wyart, J. Daillant, Can. J. Phys. 68 (9) (1990) 1084–1088.
- [31] R. Xie, A. Karim, J.F. Douglas, C.C. Han, R.A. Weiss, Phys. Rev. Lett. 81 (6) (1998) 1251–1254.
- [32] M. Tolan, O.H. Seeck, J.P. Schlomka, W. Press, J. Wang, S.K. Sinha, Z. Li, M.H. Rafailovich, J. Sokolov, Phys. Rev. Lett. 81 (13) (1998) 2731–2734.
- [33] Z. Jiang, M.K. Mukhopadhyay, S. Song, S. Narayanan, L.B. Lurio, H. Kim, S.K. Sinha, Phys. Rev. Lett. 24 (2008) 101.
- [34] M. Sikorski, C. Gutt, Y. Chushkin, M. Lippmann, H. Franz, Phys. Rev. Lett. 105 (21) (2010) 215701.